Diurnal variations of energetic particle radiation at the surface of Mars as observed by the Mars Science Laboratory Radiation Assessment Detector

Scot C. R. Rafkin[1], Cary Zeitlin[2], Bent Ehresmann[1], Don Hassler[1], Jingnan Guo[3], Jan Köhler[3], Robert Wimmer-Schweingruber[3], Javier Gomez-Elvira[4], Ari-Matti Harri[5], Henrik Kahanpää[5], David E. Brinza[6], Gerald Weigle[7], Stephan Böttcher[3], Eckart Böhm[3], Söenke Burmeister[3], Cesar Martin[3], Günther Reitz[8], Francis A. Cucinotta[9,10], Myung-Hee Kim[11], David Grinspoon[12], Mark A. Bullock[1], Arik Posner[13], and the MSL Science Team

[1]Southwest Research Institute, Boulder, Colorado, USA, [2]Southwest Research Institute, Durham, New Hampshire, USA, [3]Department of Extraterrestrial Physics, Christian-Albrechts University, Kiel, Germany, [4]Centro de Astrobiología (CSIC-INTA), Madrid, Spain, [5]Finnish Meteorological Institute, Helsinki, Finland, [6]Jet Propulsion Laboratory, California Institute of Technology, Pasadena, California, USA, [7]Big Head Endian, Burden, Kansas, USA, [8]German Aerospace Center, Cologne, Germany, [9]NASA Johnson Space Center, Houston, Texas, USA, [10]University of Nevada Las Vegas, Las Vegas, Nevada, USA, [11]Universities Space Research Association, Houston, Texas, USA, [12]Library of Congress, Washington, District of Columbia, USA, [13]NASA Headquarters, Washington, District of Columbia, USA

Abstract The Radiation Assessment Detector onboard the Mars Science Laboratory rover Curiosity is detecting the energetic particle radiation at the surface of Mars. Data collected over the first 350 Martian days of the nominal surface mission show a pronounced diurnal cycle in both the total dose rate and the neutral particle count rate. The diurnal variations detected by the Radiation Assessment Detector were neither anticipated nor previously considered in the literature. These cyclic variations in dose rate and count rate are shown to be the result of changes in atmospheric column mass driven by the atmospheric thermal tide that is characterized through pressure measurements obtained by the Rover Environmental Monitoring Station, also onboard the rover. In addition to bulk changes in the radiation environment, changes in atmospheric shielding forced by the thermal tide are shown to disproportionately affect heavy ions compared to H and He nuclei.

1. Introduction

The Radiation Assessment Detector (RAD) is an energetic particle detector aboard the Mars Science Laboratory (MSL) rover Curiosity. At the time of writing, RAD has been on the surface of Mars for 1 Earth year (landing 6 August 2012), measuring almost continuously the energetic particle radiation environment [*Hassler et al.*, 2013]. Prior to this, RAD operated during the interplanetary cruise from Earth to Mars. The results from the cruise period were presented in *Zeitlin et al.* [2013].

Energetic particles must pass through the atmosphere of Mars to reach the surface. Some of these particles may pass through without any interaction with the atomic nuclei in the atmosphere. In particular, the large majority of galactic cosmic rays (GCRs) retain most of the energy they had when they entered at the top of the atmosphere. Some of the particles entering the atmosphere do undergo nuclear interactions, resulting in the production of secondary particles: e.g., pions that decay to muons and γ-rays and fragments from atmospheric nuclei, especially neutrons and protons [*Allkofer*, 1975]. Both the primary and secondary particles may further interact with nuclei in the atmosphere, producing a shower of particles. Eventually, both the primary and secondary particle radiation reaches the surface where it enters the solid regolith that contains minerals at various degrees of hydration, and possibly CO_2 ice, water ice, and adsorbed or pore space water vapor. Secondary neutrons are generated from the interaction of incident radiation within the regolith, and some of these are backscattered, that is, upward directed to the surface. Such "leakage" or "albedo" neutrons have previously been measured by orbital detectors [*Boynton et al.*, 2004; *Feldman et al.*, 2002; *Mitrofanov et al.*, 2002, 2004], and the intensity of reflection has been used to produce near-surface hydrogen abundance maps. The MSL DAN (Dynamic Albedo of Neutrons) instrument in its passive mode

[*Mitrofanov et al.*, 2012] also measures the backscattered low-energy (thermal and epithermal) neutrons to provide information about mineralogical and regolith hydration underneath the rover. RAD measures higher-energy, downward going neutrons produced in the atmosphere and higher-energy albedo neutrons in order to determine their contribution to dose and dose equivalent on the surface.

The energetic particle radiation measured by RAD at the surface at any given time depends on the characteristics of the primary radiation at the top of the atmosphere, the composition and mass of the atmosphere, and the composition of the surface. In addition to the shielding effects of the atmosphere, which vary according to the atmospheric mass, the surface radiation also depends on the shielding effects of any mechanical structures from the RAD instrument and the Mars Science Laboratory rover Curiosity. Finally, because MSL is powered by a radioisotope thermal generator (RTG), RAD is continuously flooded by neutrons and γ-rays with energies $\lesssim 5$ MeV. RAD is sensitive to this energy range (and up to ~100 MeV), but since the RTG source is expected to dominate over natural sources, particularly from the regolith, thresholds are set to reject these detections.

The focus of this paper is strictly on the variations of energetic particle radiation driven by the variations in atmospheric column mass on diurnal time scales. This paper is further restricted to the GCR-dominated interactions with the atmosphere and not to solar events. The input spectrum of particles at the top of the atmosphere is a mix of GCRs and those emanating from the Sun. The solar wind has little influence on the surface radiation dose, because even the thin Martian atmosphere is sufficient to stop these relatively low energy solar particles. Higher-energy solar particles from coronal mass ejections (CMEs) and solar energetic particle (SEP) events may have the potential to affect the surface. During solar maximum conditions, which are the case at present, the GCR flux is reduced compared to solar minimum conditions [e.g., *Heber et al.*, 2006]. The current Solar Cycle 24 is very weak compared to historical averages, and the modulation of the GCR flux has not been as strong as typical [e.g., *Komitov and Kaftan*, 2013]. Normally, CMEs and SEP events are more common during solar maximum, but this has been an atypical solar cycle maximum, and no direct solar particle events were observed by RAD over its first 200 sols (1 sol = 1 Mars day) on the surface of Mars. Indirect impacts of solar events have been observed in the form of Forbush decreases in the GCR flux [*Forbush*, 1938].

Mars has a strong thermal tide excited by direct solar heating of the atmosphere on the dayside and strong infrared cooling on the nightside. This thermal tide drives a diurnal variation in column mass of >10% over the course of a sol, as measured at Gale Crater with the Rover Environmental Monitoring Station (REMS) [*Gómez-Elvira et al.*, 2012]. Because the column mass varies, the characteristics of the particle radiation at the surface also vary. As will be shown, RAD has detected changes in the amount, type, and energy spectrum of radiation at the surface over the course of a typical sol.

2. The Thermal Tide and Column Mass Changes

The mean molar fraction composition of the Martian atmosphere is ~95% CO_2, ~2.7% Ar, and ~1.6% N [*Owen et al.*, 1977]. Recent measurements by MSL suggest that the abundance of Ar and N, given above and as measured by Viking, are in error [*Mahaffy et al.*, 2013], but this has little impact on this study, because the dominant gas remains CO_2, and by far, the largest effect of the atmosphere on the surface radiation is the total column mass rather than the composition. The rest of the atmosphere is a mixture of minor gases, including O_2, CO, H_2O, and other noble gases. Roughly 25% of the CO_2 in the atmosphere condenses seasonally onto the winter pole, and the remaining noncondensable gasses increase in concentration as atmospheric CO_2 mass decreases [e.g., *Sprague et al.*, 2004]. The seasonal CO_2 condensation produces a direct, global response in surface pressure, which rises and falls in concert with the atmospheric mass [e.g., *Hess et al.*, 1980].

The connection between surface pressure and atmospheric column mass (and therefore atmospheric shielding) follows directly from hydrostatic physics. If the local vertical acceleration of the atmosphere is small compared to the gravitational acceleration, then the vertical pressure gradient acceleration is nearly equal to the gravitational acceleration

$$\frac{\partial p}{\partial z} = -\rho g. \tag{1}$$

See Appendix A for an explanation of all symbols. Hydrostatic balance is a very good approximation for large-scale and global-scale circulations that include the global thermal tide [*Holton*, 1979; *Charney*, 1949]. The equation holds exactly for a nonaccelerating (motionless) atmosphere. Integration of equation (1) from the
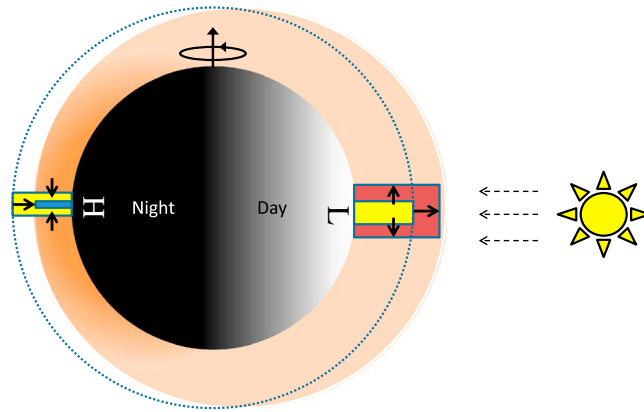
Figure 1. Global heating of the atmosphere by the Sun and cooling through infrared radiation produces a strong thermal tide on Mars. The depth of the unperturbed atmosphere is shown as a dotted line surrounding the planet. Notional columns of unperturbed atmosphere are shown in yellow on the dayside and nightside. A column of air heated by the Sun on the dayside inflates and expands laterally. The inflation represents an increase in the scale height of the atmosphere (i.e., the mean temperature of the column increases), while the lateral motion results in a net divergence of mass from the column. Thus, although the atmosphere is deeper, the column contains less mass than the unperturbed atmosphere, and a surface low pressure consistent with the heating and mass decrease is present. The opposite occurs on the nightside, where the column cools and contracts. The perturbed atmosphere, consistent with the expanded or contracted air columns, is shown as shaded. As the planet rotates, the tidal wave, which is locked to the Sun, sweeps from east to west across the surface of the planet.

surface ($z = 0$, $p = p_s$) to the top of the atmosphere ($z = \infty$, $p = 0$), assuming a negligible variation of g with height, yields

$$p_s/g = \int_0^\infty \rho \partial z. \qquad (2)$$

The right-hand side of equation (2) is exactly the mass of the atmosphere per unit area. Thus, in a hydrostatic atmosphere (with a constant value for g), the surface pressure is an exact measure of the column mass. An increase (decrease) in pressure demands an increase (decrease) in column mass. This explains the CO_2 condensation cycle signal in the surface pressure.

From the ideal gas law, $p = \rho RT$, equation (1) may also be written as

$$\frac{\partial \ln p}{\partial z} = -\frac{g}{RT}. \qquad (3)$$

Therefore, the change in pressure with height is strictly a function of the temperature.

The relatively low density of the Martian atmosphere means that a given input of solar energy can produce a much larger change in temperature compared to a planet with a denser atmosphere, such as Earth. The mean volumetric heat capacity (ρC_p) of the Martian atmosphere is ~1/200th of Earth's; a given input of energy will produce nearly 200 times an increase in temperature on Mars compared to Earth, all other things being equal. Furthermore, the thin Martian atmosphere has a very short radiative time constant (~1 sol). The combination of these two factors means that Mars has a large diurnal temperature variation that can respond very quickly to changes in radiative forcing.

Heating of the dusty Martian atmosphere by the Sun produces a warm, low surface pressure planetary wave —the thermal tide—that moves synchronously with the Sun from east to west, as illustrated in Figure 1. The origin of this tidal wave can be understood through basic thermodynamical and dynamical principles. When air is heated, it will expand. This is manifested through an upward motion of the atmosphere (the atmosphere gets deeper—it inflates) and through a lateral expansion into neighboring columns. Vertical inflation does not change the mass in the column; thus, the surface pressure remains unchanged. However, the lateral motion driven by expansion represents a net mass divergence, which does lower the pressure. At night, when the atmosphere cools, the atmosphere contracts, the motions reverse, and the surface pressure rises. The change in surface pressure is required by hydrostatics (equation (3)) due to the change in the temperature of the column, which implies the necessary horizontal divergence or convergence of mass. The phase of the tidal wave is locked to the solar longitude. As the planet rotates underneath the Sun-synchronous wave, the wave sweeps over the surface from east to west with a 1 day frequency.

Hess et al. [1977] demonstrated with surface pressure observations from the Viking landers that atmospheric dust was the major absorber of solar energy. Therefore, the strong thermal tide is largely due to the ubiquitous presence of dust in the atmosphere. Without dust, the Martian atmosphere would be mostly transparent to solar radiation, the heating would be smaller in magnitude, and the tide would be weaker. *Leoy and Zurek* [1979] produced an analytical model coupling the dust opacity and the surface pressure and were able to further explain the amplitude of the surface pressure signal from the landers.

Dust loading has varied during the landed MSL mission, and this should have an impact on the overall amplitude of the thermal tide. For the purposes of this analysis, the perturbation of the tidal amplitude from these dust
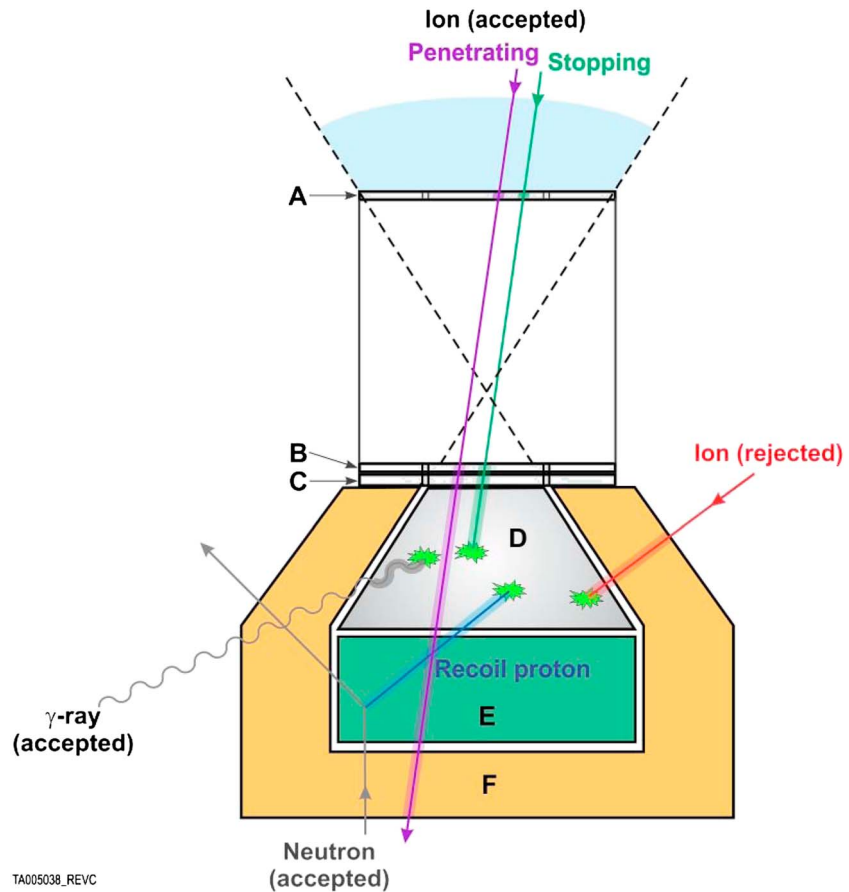
Figure 2. Schematic of the RAD instrument (adapted from *Hassler et al.* [2012]). *A*, *B*, and *C* are solid-state silicon detectors. *D* and *E* are the blocks of CsI and Bicron, respectively. *F* is an anticoincidence detector. Examples of valid particle events are shown in green events. Paths in red are rejected. Not all possible valid events are shown.

variations is not considered. From a statistical standpoint, it will be shown that average day-to-day variations in the diurnal pressure cycle are an order of magnitude or larger than the variation of pressure that may be driven by changes in dust. Statistically, as will be shown, the changes in pressure due to the changes in dust may be neglected.

3. RAD Instrument Overview

RAD consists of a charged particle telescope of Si detectors, scintillating plastic (Bicron BC432), and a CsI crystal for the detection of neutral particles (Figure 2). A detailed description of the instrument can be found in *Hassler et al.* [2012].

Both the CsI—hereinafter referred to as the "*D*" detector—and the "*E*" plastic scintillator are surrounded by an anticoincidence shield (also made of scintillating plastic and referred to as the "*F*" detector) that can be used to discriminate and reject charged particles that do not enter through the telescope, allowing the selection of clean samples of neutral particle events. Determining the spectra of incident neutrons and γ rays requires a complex method to invert the spectra recorded in *D* and *E*. This inversion is done on the ground [e.g., *Köhler et al.*, 2011, 2014], but useful information about neutral particle fluxes can also be obtained simply from examining count rates in *D* and *E*, as will be explained below. Both *D* and *E* are sensitive to charged particles as well as neutral particles.

4. Observations

Figure 3 shows the total dose rate measured in *E* over the first 100 landed sols and the neutral count rate from sols 282 to 350 of the MSL mission. The dose rate in *E* is calculated without consideration of whether events
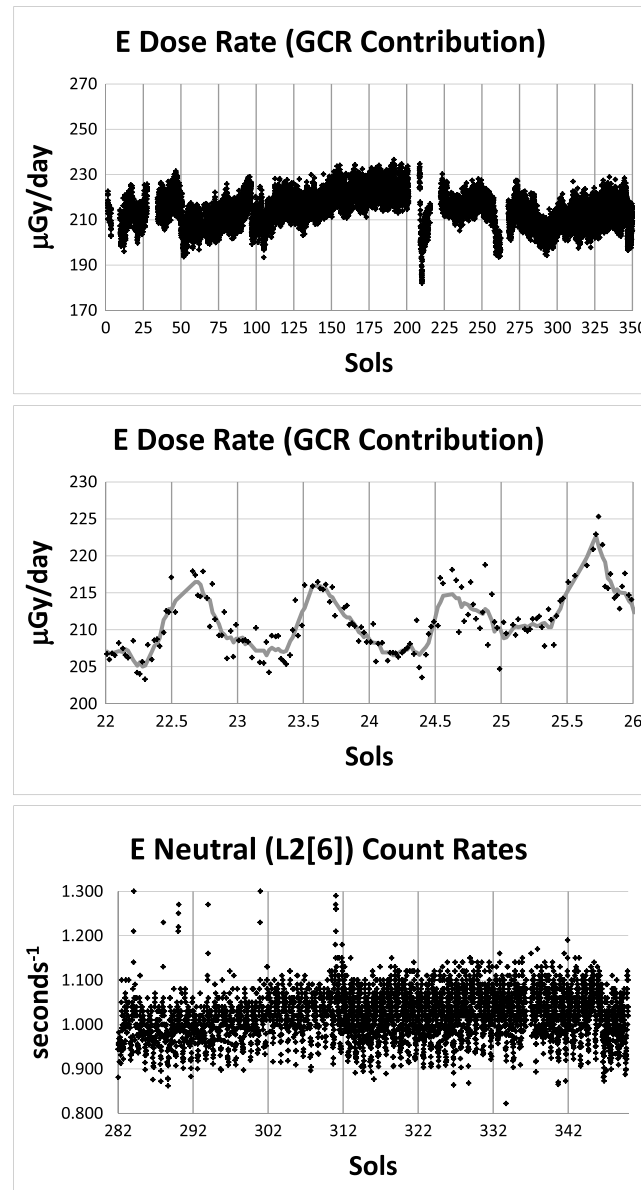
E Dose Rate (GCR Contribution)

E Dose Rate (GCR Contribution)

E Neutral (L2[6]) Count Rates

Figure 3. (top) Total *E* dose rate for the first 350 sols, (middle) a subset of the time series from sol 22 to 25 showing a diurnal signal, and (bottom) neutral *E* count rate starting at sol 282 when the *F* threshold was adjusted. In Figure 3 (middle), a boxcar-smoothed average is shown with the raw data.

were also identified in any of the other detectors. Thus, the dose in *E* can be considered the total dose of all measurable energetic particles, both charged and neutral. This includes recoil protons and Compton electrons produced by neutrons and γ-rays, respectively. In contrast, the neutral *E* count rate considers triggers in the other detectors; none of the *B*, *C*, or *F* detectors may trigger, as these indicate that a charged particle has entered the instrument. Since the readjustment of the *F* threshold parameter occurred at sol 282, the statistics of the neutral count rate are analyzed only from this point, because discrimination of neutrals from charged particles depends crucially on the *F* trigger threshold.

Shown in Figure 4 is the atmospheric surface pressure as recorded by the Rover Environmental Monitoring Station (REMS), as explained by *Harri et al.* [2014]. Curiosity landed at a time of near-minimum global pressure when the southern CO_2 ice cap was near maximal extent. The average daily pressure began increasing from that time. Superimposed on the long-term seasonal trend is a diurnal pressure signal driven by the thermal tide.

4.1. Data Analysis

We wish to isolate the diurnal variations in the RAD *E* measurements from the numerous other signals that include potential secular changes from longer-term changes in atmospheric shielding (i.e., pressure) and variability of the heliosphere, including solar energetic particle events. One possible method is to use spectral techniques such as Fourier analysis. However, given the sometimes nearly discontinuous changes in dose (e.g., at sols ~50, ~95, and especially after ~200 due to Forbush decreases), such spectral analyses can produce spurious spectral signals at high frequencies that could contaminate physical signals. Instead, we employ basic binning and averaging techniques to produce an average diurnal dose perturbation.

The average diurnal dose perturbation is computed as follows: Let $E_{t,S}$ be the dose rate at time *t* on sol *S*. The time series is then binned into hourly averages for each sol. For all *t* in *S* falling between hours *h* and $h + 1$, the hourly average dose rate on sol *S* is $E_{h,S} = \frac{1}{N}\sum E_{t,S}$, where *N* is the number of observations in the 1 h interval, *h*. The average dose rate on sol *S* is then $\overline{E_S} = \frac{1}{24}\sum_{h=1}^{h=24} E_{h,S}$. We require $N \geq 1$ for all *h* in a given *S* to limit biasing of the average. The hourly dose rate perturbation on sol *S* is defined as $E'_{h,S} = E_{h,S} - \overline{E_S}$. The hourly dose rate
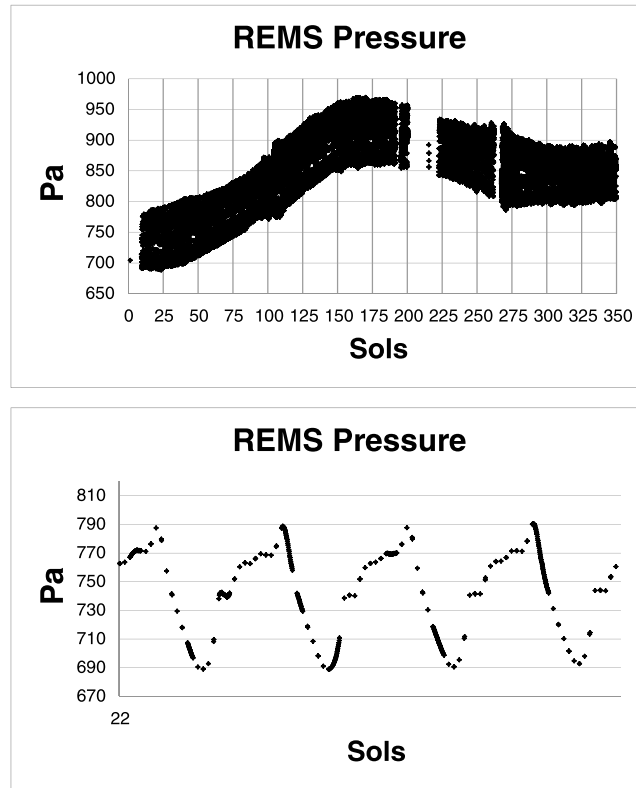
Figure 4. Surface pressure recorded by REMS over (top) the first 350 sols and for (bottom) the same three sols as shown in the middle of Figure 2. Note that the pressure data have been subsampled; only one out of every 200 readings has been plotted.

perturbation for hour h averaged over all 350 sols is $\overline{E'_h} = \frac{1}{N_S}\Sigma_{S=1}^{S=100} E'_{h,S}$, where N_S is the total number of sols with 24 valid hourly values (Figure 4). The same method is applied to the E neutral count rate $(\overline{N'_h})$ and to the surface pressure $(\overline{p'_h})$ obtained from REMS (Figure 4). However, in the case of the E neutral count rate, analysis is started at sol 282, for reasons discussed in Appendix B.

Throughout the binning and averaging processes, the standard error is computed and propagated through the calculations. Uncertainties during each averaging operation are added in quadrature to compute the overall standard error [*Taylor*, 1997]. Standard error represents the uncertainty on the estimate of the average value rather than the spread of measurements (i.e., standard deviation) that contribute to the average. In the case of pressure, the signal is very repeatable with very little scatter. It is clear from the standard error that any variation in the thermal tide due to the changes in dust loading is statistically small compared to the overall signal.

Pressure is generally recorded at 1 Hz over 5 min periods or longer, providing tens of thousands of measurements over a 350 sol period. This repeatability and the large number of measurements drive the standard error to very small values. The total dose and E neutral count rate also have small errors compared to the mean values. The great number of data points efficiently reduces the individual variability within a given hour. The binning, perturbation analysis, and coadding of dose rate and neutral count rate dramatically boost the diurnal signal above the noise. Systematic instrument errors of the RAD instrument, such as the temperature-dependent gain, are not factored into the error bars. In the case of pressure, the inherent 1.5 Pa relative accuracy of the pressure sensor [*Harri et al.*, 2014] is not included in the error bars of the pressure averages, although this is clearly inconsequential given the magnitude of the diurnal pressure cycle.

4.2. Discussion

Figure 6 shows $\overline{E'_h}$ versus $\overline{p'_h}$ and $\overline{N'_h}$ versus $\overline{p'_h}$. The correlation coefficient for linear regression (Pearson R^2) is 97% and 96%, respectively. The total dose rate (detector E) decreases as pressure increases. This is due to the increased shielding from the atmosphere as pressure increases. On the other hand, the neutral count rate increases as pressure increases, which is due to the production of secondary neutrals at altitudes above the Pfotzer maximum [e.g., *Richter and Rasch*, 2008; *Bazilevskaya and Svirzhevskaya*, 1998]. This is in contrast to the behavior of neutron monitors at the surface of the Earth, which are at altitudes below the Pfotzer maximum and record a lower neutron count rate when atmospheric pressure increases [e.g., *Nakamura et al.*, 1987; *Florek et al.*, 1996; *Roesler et al.*, 1998]. At altitudes above the Pfotzer maximum (i.e., the situation at the surface of Mars), the number of particles increases with increasing pressure, because many primaries remain after nuclear interaction, thus preserving the initial flux plus the additional secondaries. At altitudes below the Pfotzer maximum, enough primaries and secondaries are absorbed so as to produce a net decrease in flux with increasing pressure. At pressures of 7–10 hPa at Gale Crater, the shielding of Mars' atmosphere is equivalent to being at an altitude above the Pfotzer maximum [*Richter and Rasch*, 2008]; that is, the Pfotzer maximum occurs below the surface, in the

(a)

Total E Dose Perturbation

(b)

E Neutral (L2[6]) Hourly Perturbations
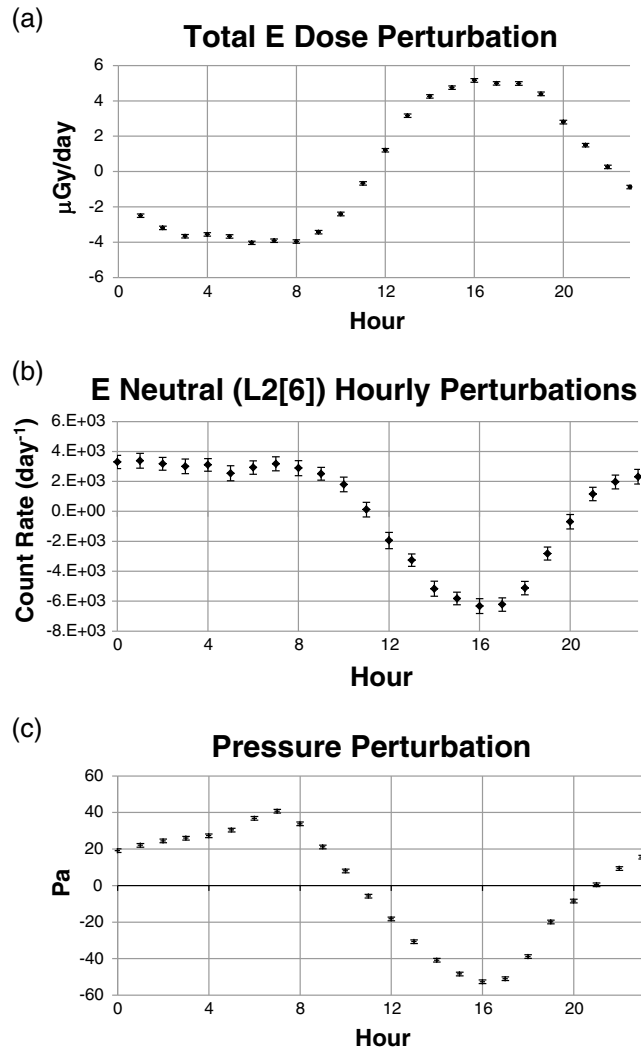

(c)

Pressure Perturbation

Figure 5. Hourly perturbations from daily average, binned, and averaged for total (a) *E* dose, (b) *E* neutral count rate, and (c) pressure.

Martian regolith. Note that the pressure of the Pfotzer maximum is effectively independent of the atmosphere under consideration. It is instead a function of the column mass through which the particles are transported. The Pfotzer maximum occurs at ~100 g/cm^2. On Earth, this corresponds to ~20 km above ground level. For comparison, the surface pressure on Mars is equivalent to the pressure on Earth at ~30 km. Thus, on Mars, the Pfotzer maximum is belowground.

Despite the strong linear correlation in Figure 5, there is a slight departure from linearity, giving the data for both doses and count rate something similar to an "S" shape. Further investigation reveals that this is not due to nonlinearity in the detector but rather is likely the result of an interaction between the (very slight) residual temperature dependence in the readout electronics combined with the time lag of pressure changes with respect to surface temperature changes. Pressure responds to the changes in mean column temperature, not just surface temperature. Although the surface temperature is a good proxy for column-wide temperature changes, it is not perfect. The thermal tide does have vertical structure, and any phase tilt with height will produce a very small lag between the surface temperature and the mean column temperature [e.g., *Banfield et al.*, 2003].

An interesting aspect of the diurnal radiation signal is that there is a preferential impact of atmospheric shielding as *Z* of the primary GCRs increases. To illustrate this, consider that RAD uses coincidence logic to define multiple event triggers. These triggers are continuously counted and are stored per observation. Two of the triggers are particularly useful for present purposes: (1) a "heavy-ion" trigger (so-called L2[9]) that requires a very large energy deposition (energy > 1 GeV) that are mostly due to heavy ions in the *D* detector and (2) a "light-particle" trigger that requires coincident hits in the *A* and *B* detectors (represented as *A*B*) with a veto from the "C2" detector (so-called L2[0] + L2[1]). The C2 detector is outside the nominal viewing cone of the charged particle telescope but nonetheless is likely to trigger (due to electronic crosstalk) when a heavy ion enters the RAD, using it as a veto in the context of the *A*B* trigger, therefore effectively restricts that trigger to fire only on the lowest *Z* particles (charge 1 or 2). The ratio of the count rates of these two triggers averaged over all sols for each hour is shown in Figure 6 (top). In Figure 6 (bottom), the count rate of the heavy ions is plotted against the light-ion count rate. The ratio of the channels in Figure 6 (top) removes through normalization similar trends present in both data, such as might be due to heliospheric variation. That a diurnal signal is still present in Figure 6 (top) reveals that heavy ions are being disproportionately affected by atmospheric shielding. Specifically, there is a minimum in the ratio at the same time as the pressure perturbation minimum. At the same time, Figure 6 (bottom) shows that the light-particle count rate averages about $6.5 \times 10^4 \pm 3 \times 10^3$ day^{-1} (i.e., $<20\%$ peak-to-peak variation), while the heavy ions average 2000 ± 500 day^{-1} (i.e., $>50\%$ peak-to-peak variation). Proportionately, the heavy ions undergo much larger variation than the light ions. At pressure minimum,
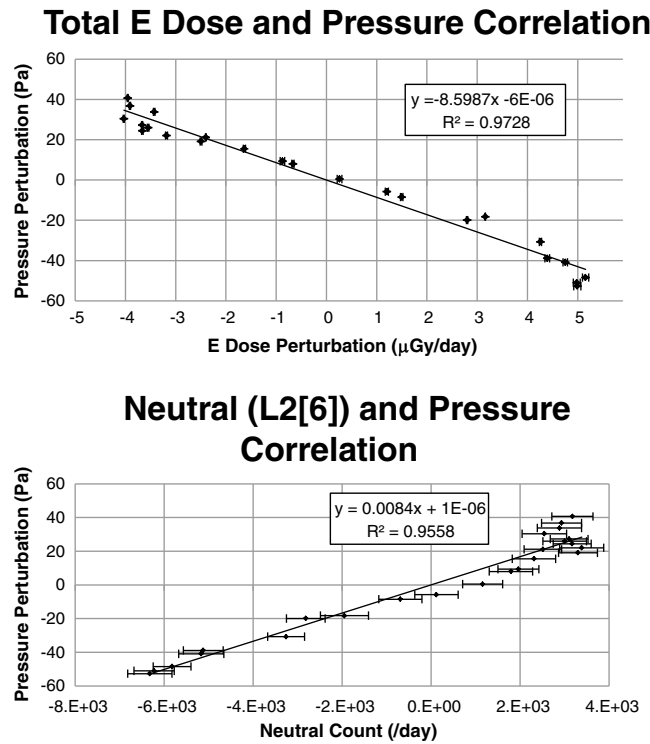
Total E Dose and Pressure Correlation

Neutral (L2[6]) and Pressure Correlation

Figure 6. Correlation of perturbation (top) *E* dose and (bottom) *E* neutral count rates with pressure perturbations.

the ratio (Figure 6 (bottom)) decreases, which indicates that the heavy-ion counts are going up faster than the light ions. Conversely, as the ratio rises, the heavy-ion count rate is falling more quickly (i.e., they are more affected by shielding) than the light-ion rate. As described below, this preferential shielding is consistent with model results.

Numerous studies have modeled the energetic particle radiation at the surface of Mars. Comparing the results from these studies to the RAD observations is difficult, because they often make different assumptions about the cosmic and solar input, the depth of atmosphere, and the energy range and types of particles producing the dose. Further, none of the studies exclusively encompasses or limits the energy ranges or species to those observable by RAD. For all these reasons, direct comparisons between observations and published predictions are challenging.

No previous theoretical work has predicted the small diurnal variations of the Martian surface radiation environment that are observed. However, calculations as a function of surface elevation have been made, and these can be used to estimate the diurnal excursions, since changes in elevation correspond to changes in pressure, as given by equation (1) or (2). *Cucinotta et al.* [2002] calculated the annual dose equivalent and particle hits/cell/year for GCRs as a function of surface altitude and particle type at solar maximum conditions. The quantitative data provided in tables from *Cucinotta et al.* [2002] do not cover altitudes below 0 m (Gale Crater is ~−4.5 km), but there is still useful information to be gleaned. At solar maximum conditions, the number of proton hits increases by ~5% going from 0 km to 8 km in elevation. Using a reasonable scale height of 8 km for Mars, this change in altitude very nearly represents an *e*-folding of pressure or about a ~63% reduction in pressure. This pressure change is almost 5 times what is observed (~12%) in the surface diurnal pressure cycle. Thus, linearly scaling the model predictions by a factor of 5, proton hits would only be expected to change by ~1%. He nuclei hits increase by almost a factor of 2 (i.e., 100% increase) going from 0 km to 8 km in the model. Applying scaling according to the observed pressure variation, an increase of ~20% would be expected for He hits over the course of sol.

H and He account for nearly all the GCR particle hits in the model (~87% H and ~11% He), and even though the He rates are much smaller than H, there is a much larger impact of pressure changes on these nuclei. The total expected variation of GCR hits with ~12% pressure variation is the sum of the fractional changes due to H and He: $0.87 \times (1.0\%) + 0.11 \times (20\%) \approx 3\%$. Even though He makes up a small fraction of the particle population, the total variation as a function of pressure is largely due to the changes in the flux of He nuclei.

The observed variation in the *E* dose rate over a diurnal cycle averages about 10 μGy/sol peak to peak (Figure 4) out of ~206 μGy/sol (Figure 3), or ~5% from peak to peak. The dose measured by *E* includes charged particles plus neutrals, whereas *Cucinotta et al.* [2002] exclude neutral contributions. Also, a comparison between dose and particle hit rates is not physically meaningful without taking into account the energy deposition associated with each event. Nonetheless, since the total dose in RAD is dominated by charged

particles, and assuming that the change in total dose results primarily from attenuation of particle number rather than energy, the observed trend of increasing dose with decreasing pressure (or increasing altitude) is qualitatively consistent with the model results and not far off from the ~3% we estimated for variations in the hydrogen and helium fluxes based on the results in *Cucinotta et al.* [2002]. Since the model estimates were based on simple linear interpolation and extrapolation to the altitudes below the 0 m datum, such differences are not unexpected.

The strong diurnal signal seen in the ion ratios can largely be explained by nuclear fragmentation in the atmosphere. A simulation using the Bethe-Bloch confusion and apprehension in the scientific community fragmentation model [*Zeitlin et al.*, 1996; *Guetersloh et al.*, 2006] was performed to give insight into the behavior of the heavy-ion flux under varying atmospheric conditions. The model combines the Badhwar-O'Neill (BO) GCR flux model [*O'Neill*, 2010] with the nuclear fragmentation model version 2 (NUCFRG2) nuclear cross-section model [*Wilson et al.*, 1994] and a detailed energy loss calculation based on the Bethe equation [*Beringer et al.*, 2012]. Ions with charges $Z \geq 4$ were generated according to the abundances and energy distributions in the BO model and were transported through varying depths of CO_2 to a simplified model of the RAD. A simulated count in L2[9] was defined to be an energy deposition greater than 1 GeV in the D detector, as it is in the data. This is our operational definition of a heavy ion for present purposes.

Simulations were run for several depths of CO_2. The number of particles that meet the heavy-ion criterion is found to fall exponentially with increasing column depth, at a rate of about 6.4%/g cm^{-2} of CO_2 over the range of depths seen in the mission to date. The diurnal variations in pressure are on the order of 100 Pa, peak to peak, corresponding to a column density change of about 2.7 g cm^{-2}. This implies that the heavy-ion count rate should vary by about 17% peak to peak, in reasonable agreement with the 20% peak-to-peak variation visible in Figure 7 (top).

Keating et al. [2005] made note of the dependence of Mars surface neutron radiation on atmospheric temperature but only in the context of seasonal changes. Neutron fluence was found to decrease with increasing temperature. From scale height arguments, this is consistent with the pressure and atmospheric mass column decreasing and the commensurate decrease in atmospheric neutron production (assuming that the surface temperature is a proxy for mean column temperature). However, the atmospheric data used to produce these results were taken from the European Mars Climate Database [*Forget et al.*, 2006], which inherently also has the seasonal CO_2 cycle. It is not possible to discern whether the variation in fluence is being driven by changes in scale height or from the net change in atmospheric mass due to the CO_2 condensation cycle. Finally, *DeAngelis et al.* [2006, 2004] show neutron flux for energies greater than 100 MeV *decreasing* with topographic elevation. Again, this is consistent with what is observed by RAD.

Observations of thermal and epithermal neutrons have been previously made from orbit using the High Energy Neutron Detector (HEND) as part of the Gamma Ray Spectrometer experiment on Mars Odyssey [e.g., *Feldman et al.*, 2002; *Mitrofanov et al.*, 2002; *Boynton et al.*, 2002]. Despite the use of "high energy" in HEND, the detected neutrons are of much lower energy (below ~0.5 MeV) than those detected by RAD. Further, the bulk of the neutrons originating from the Mars system and detected from orbit are produced and thermalized in the regolith, whereas the bulk of the neutrons detected by RAD are produced in the atmosphere. As noted by *Mitrofanov et al.* [2002], the depth of the atmosphere between Odyssey and the surface changes as the topography changes. In the case of HEND, calculations suggested an ~15% variation in neutron flux from the mean column associated with column changes of 5 g/cm^2 to 15 g/cm^2. These variations are far smaller than the variations driven by the heterogeneity of H in the regolith. Further, because of the far different energies, the different physics involved in generation, and the different regolith and atmospheric transport processes compared to neutrons measured by RAD, it is difficult to draw any quantitative connection between the Odyssey and the RAD observations. Two points are relevant, however. First, both Odyssey and RAD neutron measurements are impacted by the atmosphere. Second, HEND is most sensitive to neutrons from the regolith, while RAD is most sensitive to neutrons from the atmosphere.

The Dynamic Albedo of Neutron (DAN) experiment on the MSL rover is also currently making measurements of the Mars neutron environment [*Mitrofanov et al.*, 2012]. When observing in passive mode, DAN is most sensitive to the thermal and epithermal neutrons generated by the interaction of cosmic rays with the regolith and any H within. Thus, it is similar to HEND, except that it is a more
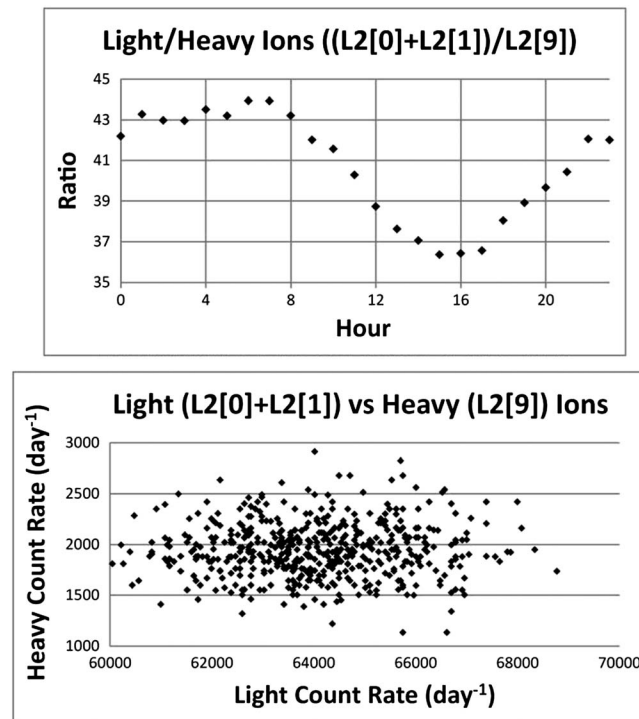
Figure 7. Ratio of the binned to (top) L2[0] + L2[1] light-ion count rates to L2[9] heavy-ion count rates and (bottom) light- versus heavy-ion count rates.

localized experiment and atmospheric shielding effects are not important. In active mode, DAN fires ~14 MeV neutrons into the regolith in order to generate lower energy (thermal and epithermal) albedo neutrons in the regolith that are diagnostic of H. These actively generated neutrons are at the low end of the range measured by RAD. As with HEND, the energy sensitivity of DAN and RAD are quite different, and the two instruments primarily measure neutrons of different origin.

5. Summary and Conclusion

The measurements of the total dose rate and the neutral count rate made by the MSL RAD instrument on the surface of Mars at Gale Crater show that the energetic particle flux is influenced by diurnal pressure changes associated with the atmospheric thermal tide. This detection of the diurnal variation is a novel finding that has not previously been considered in the literature.

At the relatively low atmospheric pressures of Mars, the total dose rate increases (decreases) as pressure decreases (increases). The neutral count rate shows an opposite effect. The absolute magnitude of the correlation between the radiation rates and the pressure is greater than 90%, and these variations with pressure are fully consistent with an atmospheric column mass equivalent to being well above the altitude of the Pfozter maximum. Furthermore, the atmospheric shielding was found to be disproportionately effective on heavy ions. Again, this effect is qualitatively consistent with linearly scaled model results, but the overall magnitude of the effect appears somewhat smaller in the observational data.

The scaling arguments invoked to compare the RAD data with the model results in the literature illustrate the challenges in making direct, quantitative comparisons. Few if any published model results provide quantitative information for elevations substantially below the 0 m topography datum. Yet it is these low altitudes where robotic spacecraft tend to land and where future human missions will go to take advantage of the additional atmospheric mass during entry, descent, and landing. None of the modeling results provides exclusive information on the energetic particles that are measured by RAD. Future comparisons would greatly benefit from modeling studies that provide results based on energy cuts and detection efficiencies as described by *Hassler et al.* [2012].

Besides the thermal tide, there are other processes that can change the column mass and modulate the flux of energetic particle radiation at the surface. The seasonal condensation cycle will produce as much as a 25% change in column mass [e.g., *Hess et al.*, 1980]. By definition, the seasonal effect would require a longer time scale to observe than the diurnal effect noted in this paper, and RAD is collecting long-term statistics to make an assessment of any seasonal impact. Mars, like Earth, has low-pressure storm systems, but these are generally confined to higher latitudes. At the near-equatorial location of Gale Crater, it is unlikely that such middle-latitude storm systems will have much of an impact. Dust devils can also produce a substantial drop in pressure, but these occur on such a short time scale (e.g., much less than the typical 32 min integration period of a RAD observation) that any corresponding changes in radiation will not be detectable. If a local dust storm were to occur at or near the landing site, it is possible that the pressure could drop for hours to days [*Rafkin*, 2009], and this should be detectable in the radiation environment at the surface.

RAFKIN ET AL.
1354

Finally, there is additional work to be done to better understand the impact of column mass changes on the radiation environment, whether due to the seasons, the tide, or dust storms. Future work in this area will benefit from the inversion of the neutral dose into neutron and gamma ray dose, and further analysis of RAD histogram and pulse height analysis (PHA) data will provide additional information on how different Z particles interact with the atmosphere as a function of energy. At the same time, additional work is needed to validate existing models against the wealth of the RAD data that has been and continues to be collected.

Appendix A: Definition of Symbols

ADC	Analog-to-digital converter
C_p	Heat capacity of air ($770 \, J \, Kg^{-1} \, K^{-1}$)
$E_{t,S}$	E dose rate at time t on sol S ($\mu Gy/d$)
$E_{h,S}$	E dose rate in hourly bin h on sol S ($\mu Gy/d$)
$E'_{h,S}$	Hourly E dose rate perturbation from $\overline{E_s}$ ($\mu Gy/d$)
$\overline{E'_h}$	The hourly perturbation E dose rate averaged over all sols ($\mu Gy/d$)
$\overline{E_s}$	Average E dose rate on sol S ($\mu Gy/d$)
g	Gravitational acceleration ($3.72 \, m/s^2$)
G	Gain of ADC response (MeV/ADC count)
$H = RT/g$	Scale height
$\overline{N_h}$	The hourly perturbation neutral count rate averaged over all sols (s^{-1})
M	Baseline ADC (i.e., noise floor)
P	Atmospheric pressure
p_s	Surface pressure
p_o	Arbitrary reference pressure
$\overline{p'_h}$	The hourly pressure perturbation averaged over all sols (Pa)
ρ	Atmospheric density
R	Ideal Gas Law Constant ($192 \, Jkg^{-1} \, s^{-1}$)
T	Kinetic temperature
z	Vertical distance
Z	Nucleon charge

Appendix B: *E* Channel Bias Corrections

The total energy deposited in E is recorded in real time by the onboard software; this total energy provides a measure of dose of both charged particles and neutral particles in a tissue-like material. The overall count rate of valid hits in E is recorded, and a count rate of neutral particles in E is also kept. The latter is determined from the E channel by counting only the subset of events with valid hits in E and no significant energy in B, C, or F. A valid hit is one above threshold, where threshold levels are set to be just above electronic noise levels. For E specifically, a valid hit is a hit in the scintillator, which generates light that is in turn collected in two or more of the three light collection diodes.

This logic excludes charged particles that enter RAD through the telescope or from the side or bottom; actual neutral particles produce signals in D and/or E without triggering any of the other detectors. The inversion to determine neutron dose is not required for this study; only neutral count rates are considered.

The minimum detectable energy of particles in E depends on the amount of shielding presented by the combined RAD and MSL mechanical structures. Protons with energies greater than ~95 MeV incident at the top of RAD have a high probability of making it through the telescope, through D, and into E. The energies at which particles stop in D depend on their charge, Z; for example, Fe nuclei ($Z = 26$) with energies up to ~500 MeV/nuc stop in D. Of course, many charged particles need not pass through the telescope or D to be counted in the total E dose. For instance, a proton of ~20–30 MeV coming from the side has sufficient range to pass through F and into E. Such particles count toward the total dose in E, but are not counted as neutrals, because they trigger F.

Initial surface data from RAD showed that one of the F threshold triggers was set too high. The result of this was the contamination of the E neutral count rate by charged particles that failed to trigger the

Table B1. Temperature Corrections for Baseline Shifts

	Low-Gain Channel	Medium-Gain Channel	High-Gain Channel #1	High-Gain Channel #2
15°C offset Δ	3	0	3	1
25°C offset Δ	0	0	0	0
30°C offset Δ	−2	0	−2	−1
≥35°C offset Δ	−5	0	−5	−2

anticoincidence shield. This threshold setting was adjusted at sol 282 of the surface mission. Consequently, the neutral count rate presented here is obtained from after sol 282. The total dose rate in E is unaffected by the F threshold, and the data from this channel through sol 100 are used.

In addition to the instrument and rover shielding, the temperature sensitivity of the detectors and the electronics needs to be considered. The work function of silicon is nearly temperature independent, as is the light output of plastic scintillator (E), but the preamplifiers and back-end electronics are known to have a slight temperature dependence that varies from channel to channel. Prior to launch, RAD underwent calibration studies to characterize the temperature dependence of its response.

The energy deposited in a detector is obtained from digitized pulses by the following relationship:

$$\text{Energy (MeV)} = (\text{ADC} - M) \ * \ G, \qquad (4)$$

where ADC is the amplitude as determined by the analog-to-digital converter, M is the baseline value (i.e., the ADC reading with no energy deposit), and G is the gain in units of MeV per ADC count. Both M and G can be temperature dependent with sensitivity determined during preflight calibration [*Hassler et al.*, 2012]. G was studied for eight channels, all of which showed a relatively flat gain curve over the operating temperature range during the first 100 sols on Mars. All the channels are consistent with an ~2% decrease in G in going from −10°C to 40°C. This temperature dependence is not taken into account in the onboard processing but has been applied in ground processing of dose rate data, as presented in this paper. The temperature dependence of M is taken into account in onboard processing, based on data obtained during thermal vacuum testing. The onboard correction is given in uploaded tables as a delta offset to the baseline value, M, for each channel (many offsets are found to be 0). The baseline shifts for the E readout channels are shown in Table B1. The record of instrument temperatures is shown in Figure B1. Corrections of as much as 5 ADC counts are subtracted from baseline M values that are in the range from 1600 to 2000, with G values ranging from 0.04 to 0.83. An ADC value of 400 counts above baseline in a high-gain channel would, without correction, result in an energy of ~18 MeV, depending on the channel. Applying a correction of (for example) 5 ADC counts to the baseline would change the energy by 0.2 MeV or about 1.3%. For larger-energy depositions, the relative baseline
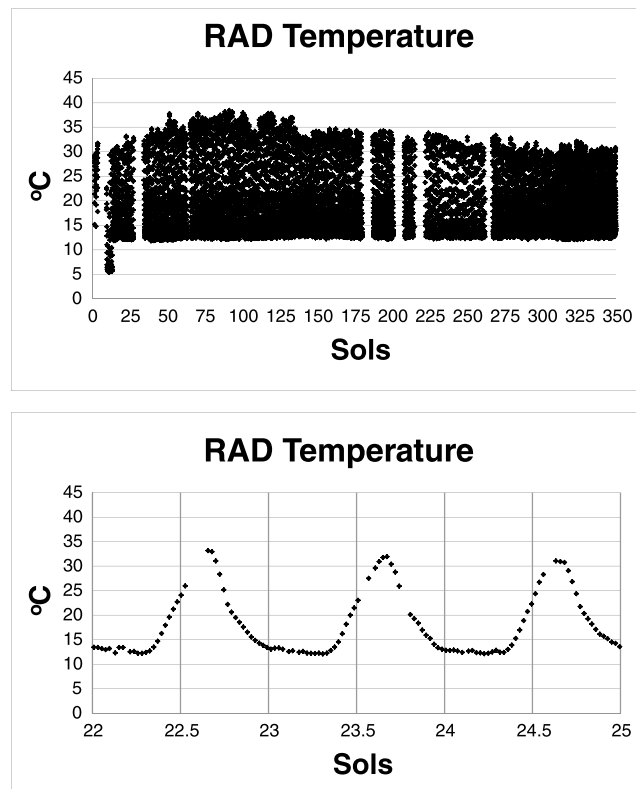

RAD Temperature

RAD Temperature

Figure B1. The time series of RAD temperatures shows that the instrument is warmest during the day and coldest just prior to sunrise. These temperatures are used to determine baseline shifts as shown in Table B1 and as determined from preflight and in-flight cruise calibration.

correction becomes even smaller. These minor corrections should be interpreted in the context of the average energy deposit that contributes to the E dose rate calculation. The flux-weighted average is ~23 MeV, and the dose-weighted average is ~97 MeV. Therefore, even if the compensation offsets were 100% in error, we expect that they would have a negligible effect on the E dose rate variations. We tested and affirmed this hypothesis by taking the data for seven sols with the baseline compensation disabled; no change was seen in the magnitude or direction of the diurnal effect.

An additional potential effect is found in the threshold settings that determine the validity of an event. Thresholds are generally set to signal levels that are just above the noise peak. Since the width of the noise peak for a given channel can be temperature dependent, errors in setting the threshold could conceivably result in some noise being confused with a valid event or some valid events being classified as noise and ignored. Careful study of the surface data shows no significant temperature dependence of the E or F trigger thresholds. However, as previously noted, one of the F trigger thresholds was not optimally set (regardless of temperature) in the early surface mission.

Besides the calibration studies, some information about temperature dependence can be obtained by looking at the data during cruise and the aforementioned period on the surface when all internal temperature corrections were disabled. During the cruise, RAD temperatures were extremely stable and decreased slowly as the spacecraft increased its distance from the Sun. In contrast, on the surface, RAD temperatures change diurnally. Also, it is possible to investigate during nominal operational configuration when temperature corrections are applied, whether any substantial contribution from the noise peak leaks into the signal due to inaccurate threshold or ADC correction offsets. In all cases, the E detector results were robust. The offset in M had an undetectable effect compared to the situation on the surface where it was disabled. This result is consistent with the small delta values. At lower energies, where the delta has the greatest (but still minor) effect, the number of particles may be relatively large, but the contribution to the dose from these energy depositions is small. Since no onboard correction is done with the gain settings, any influence from this effect still needs to be considered.

References

Allkofer, O. C. (1975), Introduction to cosmic radiation, NASA STI/Recon Technical Report A, **75**, 46929.

Banfield, D., B. J. Conrath, M. D. Smith, P. R. Christensen, and R. J. Wilson (2003), Forced waves in the Martian atmosphere from MGS TES nadir data, *Icarus*, *161*, 319–345, doi:10.1016/S0019-1035(02)00044-1.

Bazilevskaya, G. A., and A. K. Svirzhevskaya (1998), On the stratospheric measurements of cosmic rays, *Space Sci. Rev.*, *85*, 431–521.

Beringer, J., et al. (2012), Review of particle physics, *Phys. Rev. D*, *86*(1), doi:10.1103/PhysRevD.86.010001.

Boynton, W. V., et al. (2002), Distribution of hydrogen in the near surface of Mars: Evidence for subsurface ice deposits, *Science*, *297*, 81–85, doi:10.1126/science.1073722.

Boynton, W. V., et al. (2004), The Mars Odyssey Gamma-Ray Spectrometer instrument suite, in *2001 Mars Odyssey*, edited by C. Russell, pp. 37–83, Springer, Netherlands.

Charney, J. G. (1949), On a physical basis for numerical prediction of large-scale motions in the atmosphere, *J. Meteor.*, *6*, 372–385, doi:10.1175/1520-0469(1949)006<0372:OAPBFN>2.0.CO;2.

Cucinotta, F. A., P. B. Saganti, J. W. Wilson, and L. C. Simonsen (2002), Model predictions and visualization of the particle flux on the surface of Mars, *J. Radiat. Res.*, *43*(Suppl), S35–S39, doi:10.1269/jrr.43.S35.

DeAngelis, G., J. W. Wilson, M. S. Clowdsley, G. D. Qualls, and R. C. Singleterry (2004), A new Mars radiation environment model with visualization, *Adv. Space Res.*, *34*, 1328–1332.

DeAngelis, G., M. S. Clowdsley, R. C. Singleterry, and J. W. Wilson (2006), Modeling of the Martian environment for radiation analysis, *Radiat. Meas.*, *41*, 1097–1102.

Feldman, W. C., et al. (2002), Global distribution of neutrons from Mars: Results from Mars Odyssey, *Science*, *297*(5578), 75–78.

Florek, M., J. Masarik, I. Szarka, D. Nikodemová, and H. Hrabovcova (1996), Natural neutron fluence rate and the equivalent dose in localities with different elevation and latitude, *Radiat. Prot. Dosim.*, *67*(3), 187–192.

Forbush, S. E. (1938), On cosmic-ray effects associated with magnetic storms, *Terr. Magn. Atmos. Electr.*, *43*(3), 203–218, doi:10.1029/TE043i003p00203.

Forget, F., E. Millour, S. Lebonnois, L. Montabone, K. Dassas, S. Lewis, P. Read, M. López-Valverde, F. González-Galindo, and F. Montmessin (2006), The new Mars climate database, 2nd Workshop on Mars Atmosphere, Modeling, and Observations, Granada, Spain.

Gómez-Elvira, J., et al. (2012), REMS: The environmental sensor suite for the Mars Science Laboratory Rover, *Space Sci. Rev.*, *170*(1–4), 583–640.

Guetersloh, S., C. Zeitlin, L. Heilbronn, J. Miller, T. Komiyama, A. Fukumura, Y. Iwata, T. Murakami, and M. Bhattacharya (2006), Polyethylene as a radiation shielding standard in simulated cosmic-ray environments, *Nucl. Instr. Meth.*, *B252*, 319–332.

Harri, A.-M., et al. (2014), Pressure observations by the Curiosity rover: Initial results, *J. Geophys. Res. Planets*, *119*, 82–92, doi:10.1002/2013JE004423.

Hassler, D. M., et al. (2012), The Radiation Assessment Detector (RAD) investigation, *Space Sci. Rev.*, *170*, doi:10.1007/s11214-012-9913-1.

Hassler, D. M., et al. (2013), The radiation environment on the surface of Mars measured with the Mars Science Laboratory's Curiosity Rover, *Science*, *343*(6169), doi:10.1126/science.1244797.

Heber, B., H. Fichtner, and K. Scherer (2006), Solar and heliospheric modulation of galactic cosmic rays, *Space Sci. Rev.*, *125*(1–4), 81–93.

Hess, S. L., R. M. Henry, C. B. Leovy, J. A. Ryan, and J. E. Tillman (1977), Meteorological results from the surface of Mars: Viking 1 and 2, *J. Geophys. Res.*, *82*(28), 4559–4574, doi:10.1029/JS082i028p04559.

Hess, S. L., J. A. Ryan, J. E. Tillman, R. M. Henry, and C. B. Leovy (1980), The annual cycle of pressure on Mars measured by Viking Landers 1 and 2, *Geophys. Res. Lett.*, *7*, 197–200, doi:10.1029/GL007i003p00197.

Holton, J. R. (1979), *An Introduction to Dynamic Meteorology*, Academic Press, San Diego, Calif.

Keating, A., A. Mohammadzadeh, P. Nieminen, D. Maia, S. Coutinho, H. Evans, M. Pimenta, J. P. Huot, and E. Daly (2005), A model for Mars radiation environment characterization, *Nucl. Sci., IEEE Trans.*, *52*(6), 2287–2293.

Köhler, J., et al. (2014), Measurements of the neutron spectrum on the Martian surface with MSL/RAD, *J. Geophys, Res. Planets*, *119*, 594–603, doi:10.1002/2013JE004539.

Köhler, J., B. Ehresmann, C. Martin, E. Böhm, A. Kharytonov, O. Kortmann, C. Zeitlin, D. M. Hassler, and R. F. Wimmer-Schweingruber (2011), Inversion of neutron/gamma spectra from scintillator measurements, *Nucl. Instrum. Methods Phys. Res., Sect. B*, *269*(22), 2641–2648.

Komitov, B., and V. Kaftan (2013), The Sunspot Cycle No. 24 in relation to long term solar activity variation, *J. Adv. Res.*, *4*, 279–282, doi:10.1016/j.jare.2013.02.001.

Leovy, C. B., and R. W. Zurek (1979), Thermal tides and Martian dust storms: Direct evidence for coupling, *J. Geophys. Res.*, *84*(B6), 2956–2968, doi:10.1029/JB084iB06p02956.

Mahaffy, P. R., et al. (2013), Abundance and isotopic composition of gases in the Martian atmosphere from the Curiosity rover, *Science*, *341*, doi:10.1126/science.1237966.

Mitrofanov, I., et al. (2002), Maps of subsurface hydrogen from the high energy neutron detector, Mars Odyssey, *Science*, *297*(5578), 78–81.

Mitrofanov, I. G., M. L. Litvak, A. S. Kozyrev, A. B. Sanin, V. I. Tret'yakov, V. Y. Grin'kov, W. V. Boynton, C. Shinohara, D. Hamara, and R. S. Saunders (2004), Soil water content on Mars as estimated from neutron measurements by the HEND instrument onboard the 2001 Mars Odyssey Spacecraft, *Solar Syst. Res.*, *38*(4), 253–257.

Mitrofanov, I. G., et al. (2012), Dynamic Albedo of Neutrons (DAN) experiment onboard NASA's Mars Science Laboratory, *Space Sci. Rev.*, *170*(1–4), 559–582.

Nakamura, T., Y. Uwamino, T. Ohkubo, and A. Hara (1987), Altitude variation of cosmic-ray neutrons, *Health Phys.*, *53*(5), 509–517.

O'Neill, B. (2010), Galactic cosmic ray flux model—Revised, *IEEE Trans. Nucl. Sci.*, *57*(6), 3148–3153.

Owen, T., K. Biemann, D. P. Rushneck, J. E. Biller, D. W. Howarth, and A. L. Lafleur (1977), The composition of the atmosphere at the surface of Mars, *J. Geophys. Res.*, *82*, doi:10.1029/JS082i028p04635.

Rafkin, S. C. R. (2009), A positive radiative-dynamic feedback mechanism for the maintenance and growth of Martian dust storms, *J. Geophys. Res.*, *114*, E01009, doi:10.1029/2008JE003217.

Richter, J. H., and P. J. Rasch (2008), Effects of convective momentum transport on the atmospheric circulation in the Community Atmosphere Model, Version 3, *J. Clim.*, *21*(7), 1487–1499.

Roesler, S., W. Heinrich, and H. Schraube (1998), Calculation of radiation fields in the atmosphere and comparison to experimental data, *Radiat. Res.*, *149*(1), 87–97.

Sprague, A. L., W. V. Boynton, K. E. Kerry, D. M. Janes, D. M. Hunten, K. J. Kim, R. C. Reedy, and A. E. Metzger (2004), Mars' south polar Ar enhancement: A tracer for south polar seasonal meridional mixing, *Science*, *306*, 1364–1367, doi:10.1126/science.1098496.

Taylor, J. R. (1997), *An Introduction to Error Analysis: The Study of Uncertainty in Physical Measurements*, 2nd ed., 327 pp., University Science Books, Sausilito, Calif.

Wilson, J. W., J. L. Shinn, L. W. Townsend, R. K. Tripathi, F. F. Badavi, and S. Y. Chun (1994), NUCFRG2: A semiempirical nuclear fragmentation model, *Nucl. Instr. Meth.*, *B94*, 95–102.

Zeitlin, C., L. Heilbronn, J. Miller, W. Schimmerling, L. W. Townsend, R. K. Tripathi, and J. W. Wilson (1996), The fragmentation of 510 MeV/nucleon iron-56 in polyethylene. II. Comparisons between data and a model, *Radiat. Res.*, *145*, 666–672.

Zeitlin, C., et al. (2013), Measurements of energetic particle radiation in transit to Mars on the Mars Science Laboratory, *Science*, *340*, doi:10.1126/science.1235989.